



Synchrotron Characterisation of Ultra-Fine Grain TiB₂/Al-Cu Composite Fabricated by Laser Powder Bed Fusion

Sheng Li¹ · Biao Cai¹ · Ranxi Duan^{1,2} · Lei Tang¹ · Zihan Song¹ · Dominic White³ · Oxana V. Magdysyuk⁴ · Moataz M. Attallah¹

Received: 15 June 2021 / Revised: 26 July 2021 / Accepted: 4 August 2021 / Published online: 29 September 2021
© The Author(s) 2021

Abstract

Isotropy in microstructure and mechanical properties remains a challenge for laser powder bed fusion (LPBF) processed materials due to the epitaxial growth and rapid cooling in LPBF. In this study, a high-strength TiB₂/Al-Cu composite with random texture was successfully fabricated by laser powder bed fusion (LPBF) using pre-doped TiB₂/Al-Cu composite powder. A series of advanced characterisation techniques, including synchrotron X-ray tomography, correlative focussed ion beam–scanning electron microscopy (FIB-SEM), scanning transmission electron microscopy (STEM), and synchrotron in situ X-ray diffraction, were applied to investigate the defects and microstructure of the as-fabricated TiB₂/Al-Cu composite across multiple length scales. The study showed ultra-fine grains with an average grain size of about 0.86 μm, and a random texture was formed in the as-fabricated condition due to rapid solidification and the TiB₂ particles promoting heterogeneous nucleation. The yield strength and total elongation of the as-fabricated composite were 317 MPa and 10%, respectively. The contributions of fine grains, solid solutions, dislocations, particles, and Guinier–Preston (GP) zones were calculated. Failure was found to be initiated from the largest lack-of-fusion pore, as revealed by in situ synchrotron tomography during tensile loading. In situ synchrotron diffraction was used to characterise the lattice strain evolution during tensile loading, providing important data for the development of crystal-plasticity models.

Keywords Aluminium metal matrix composite · Laser powder bed fusion · Heterogeneous nucleation · Synchrotron characterisation

1 Introduction

Laser powder bed fusion (LPBF), an additive manufacturing (AM) technique, uses a laser to melt and fuse the powder selectively to form a 3D structure in a layer-by-layer fashion [1–3]. The development of LPBF enables the rapid production of complex components based on computer-aided design models. To meet the growing demand for lightweight components in the automotive and aerospace sectors, many researchers have used LPBF to fabricate high-performance aluminium (Al) alloys and composites. A variety of Al-alloys have been successfully printed using LPBF, including Al-Si [4], Al-Si-Mg [5, 6], Scalmalloy [7, 8], Al-Mn-Sc [9, 10], Al-Mg-Si-Sc [11, 12], Al-Cu [13, 14] and Al-matrix composites [15–17].

One of the major challenges facing LPBF of Al alloys is to suppress the defects and detrimental microstructures, such as hot tearing and columnar grains, mostly related to the steep thermal gradients in the confined melt pool and the rapid

Available online at <http://link.springer.com/journal/40195>

✉ Biao Cai
b.cai@bham.ac.uk

✉ Moataz M. Attallah
M.M.Attallah@bham.ac.uk

¹ School of Metallurgy and Materials, University of Birmingham, Edgbaston, Birmingham B15 2TT, UK

² Department of Materials Science and Engineering, Southern University of Science and Technology, Shenzhen 518055, China

³ ZEISS House, Building 1030, Cambourne Business Park, Cambourne, Cambridge CB23 6DW, UK

⁴ Diamond Light Source Ltd, Harwell Science and Innovation Campus, Didcot OX11 0DE, Oxfordshire, UK

solidification associated with laser heating [2, 9, 11, 18–24]. This is the main reason why there is a limited number of Al alloys that can be fabricated by LPBF. One promising solution to improve the processability of Al-alloys is to dope the alloys with nanosized high melting point particles, such as TiB₂, SiC, TiN, and TiC [17, 25–28], which benefits the material in three ways. Firstly, the particles can act as sites for heterogeneous nucleation during solidification, leading to ultra-fine grains, and avoiding columnar grains [29, 30]. Secondly, as fine grains are introduced, the strain caused by volumetric solidification shrinkage and thermal contraction can be accommodated within the semi-solid state, preventing the formation of hot tearing [28]. Finally, the nanoparticles introduced and the fine equiaxed grains formed are both beneficial to the mechanical performance [31].

To date, there are several methods to introduce nanoparticles to Al alloys. One approach is to decorate nanoparticles onto the surface of the Al-powder as nucleation sites for α -Al grains [32–34]. For instance, Martin et al. [28] coated 7075 and 6061 alloy powders with nano-ZrH₂ [28]. Recently, Tan et al. [35] mixed 2024 Al alloy powders with Ti nanoparticles, and fine-grained 2024 alloy was successfully fabricated by LPBF. The composite produced by mixed powder shows mechanical properties close to that of wrought 2xxx series alloys [17, 29, 36]. Another approach is to pre-dope the Al-alloy with nanoparticles. Ghoncheh et al. produced TiB₂ pre-doped A205 alloys via LPBF [37]. Li et al. [38] fabricated Al-10Si-Mg ingot reinforced with TiB₂ nanoparticles using a salt-metal reaction method. The ingot was then used to produce powders by gas-atomisation. This led to exceptionally high-strength Al alloys and good ductility. However, the influence of nanoparticle size on grain formation remains further study. The distribution of defects, TiB₂ and precipitates, and failure mechanism significantly affect the properties of LPBFed TiB₂/Al-Cu composite, but is difficult to be studied via traditional methods. By utilising the advantage of synchrotron in situ testing and advanced microscopes, our study produced Al-Cu-based powders pre-doped with TiB₂ particles for the LPBF process and investigated the defects, formation of fine grains, distribution of particles, and their behaviours during deformation.

In this study, the LPBF printed TiB₂/Al-Cu composite with good mechanical properties comparable to that of Al-Cu-based cast and wrought products, was successfully printed by LPBF. A comprehensive analysis was performed to understand its microstructure, mechanical properties, and failure mechanisms. The mechanical performance of the printed TiB₂/Al-Cu composite originates from its microstructure. Hence, it is important to map the distribution of defects, the hierarchical microstructure, and their influence on the deformation behaviour of the composite. We used high-resolution synchrotron computed tomography (CT), 3D scanning electron microscope (3D-SEM), and scanning

transmission electron microscopy (STEM) characterisation to analyse porosity, grain structure, secondary particles, and nanoprecipitation. Additionally, in situ synchrotron CT and diffraction were used during tensile loading [5, 39, 40] to probe the micro-mechanical properties and failure mechanisms of LPBF printed composite at the I12 beamline diamond light source. The detailed characterisation and in situ tests allowed us to establish the multi-scales architecture of the TiB₂/Al-Cu composite, which significantly facilitates the understanding of the structure–properties relationship of the composite.

2 Experimental

2.1 Materials and Process Parameters

Pre-doped TiB₂/Al-Cu alloy electrode induction gas atomisation powder, which contains 4–6 wt% Cu, around 0.2–0.4 wt% Mg, around 0.5–1 wt% Ag, 2–3 wt% Ti and 0.7–1 wt% B, was provided by TLS Technik GmbH & Co. Spezialpulver KG, Germany, with particle size between 15 and 53 μ m. Solid samples were fabricated by an SLM500HL LPBF machine (SLM solution GmbH, Germany) under argon atmosphere (less than 0.01% oxygen content), using an 80 μ m diameter Gaussian laser beam. The processing parameters were 360 W power, 1500 mm/s scan speed, 0.15 mm hatch spacing and 30 μ m layer thickness. The platform was heated up to 150 °C before LPBF processing and kept during the processing. The use of the platform preheat aims to reduce the residual stresses associated with LPBF, while facilitating the powder spreadability by removing any moisture. The scan strategy used in this study was 10 mm width strip scans and the 90° strip rotation between layers. The building direction (BD) was defined as the Z direction. The machine runs on a full-powder recycling system using a sieving station and an extruder powder delivery system. Thus, some irregular-shaped partial melt powders and spatter particles were occasionally observed. The recycled powders were collected from the powder tank before the build started, and spatter particles were collected from the downwind side of the build chamber after the build finished.

2.2 Metallurgy Preparation and Mechanical Testing

The samples for microstructure analysis and in situ tensile testing were cut from a 30 mm \times 20 mm \times 30 mm block, via electrical discharge machining (EDM) and then were ground by sandpapers and polished by both 3 μ m and 0.05 μ m diamond suspension, followed by microstructural investigations.

Three M8 tensile bars with 20 mm gauge length and 4 mm gauge diameter were tested using an ESH tensile

testing machine to obtain the stress–strain curve according to the ASTM-E8 standard [41]. The geometries of the in situ tensile and ASTM-E8 samples are provided in the supplementary note. The loading direction of both in situ and standard tensile tests was paralleled to the BD (Z direction). The details of sample geometry can be found in supplementary materials.

2.3 Electron Microscopy

The as-fabricated samples were then characterised using a ZESIS crossbeam 550 FIB-SEM, after locating the defects from the X-ray computed tomography (CT) results. During the milling, secondary and backscatter images were taken from 785 sections with 14 nm slice intervals, using 1.5 kV, 5 nA beam and a pixel size of 10 nm. Meanwhile, 75 energy-dispersive spectroscopy (EDS) maps with 100 nm pixel size were taken from the investigated volume with 140-nm slice intervals.

SEM imaging and electron backscattered diffraction (EBSD) mapping were acquired using TESCAN Mira3 SEM, Czech Republic. The step size of EBSD mapping was 0.1 μm . The acquisition rate was higher than 80%, and the post-processing was done by MTEX software [42]. The inverse pole figure (IPF) map was processed using the filling missing function. The grain boundary angle $> 15^\circ$ was defined as a large angle grain boundary, and the grain size less than three times of step size (less than 0.3 μm) was eliminated as noise. The pole figure analysis was done on raw data without post-processing. The transmission electron microscopy (TEM) investigation was performed using a Tecnai F30 (FEI, USA), operated at 300 kV. The high-angle annular dark-field scanning TEM (HAADF-STEM) characterisation was done using an FEI Talos TEM at 200 kV. The TEM samples were prepared via mechanical grinding, polishing and ion milling (PIPSTM, Gatan, Inc., USA).

2.4 In Situ Synchrotron Characterisation

In situ X-ray diffraction and CT were performed at the I12 beamline of Diamond Light Source, UK [43]. The Deben CT5000 micromechanical testing machine was used for in situ tensile loadings. The in situ tests were conducted on a flat dog-bone tensile sample with 1.8 mm width and 10 mm length gauge (see supplementary). The energy of the monochromatic beam was 53.7 keV (wavelength of 0.23088 \AA). For tomographic imaging, pco.edge 5.5 CMOS detector was used with module four optics at a sample-to-detector distance of 0.55 m. Each tomogram comprised a total of 1800 equally spaced radiographs over a 180° rotation with 0.5 ms exposure. All tomograms were reconstructed with Savu software [44–46]. The voxel size of the tomograms was 1.3 μm . The X-ray diffraction pattern was acquired

using Pilatus 2 M CdTe detector, positioned at a distance of 0.742 m from the specimen and calibrated with a CeO_2 powder sample using DAWN software [47–49]. The beam size of $200 \mu\text{m} \times 200 \mu\text{m}$ was used with 1 s exposure time. The noise reduction filter was set at 3 pixel size; therefore, the minimum recognisable pore size in this technique is 3.9 μm . Tomograms and diffraction patterns were captured alternatively on the same sample, as the load increased. The changeover between tomography and diffraction at load steps of interest was achieved by the movement of the detector and beam-stop stages.

For diffraction data analysis, the azimuthal integrations of 15° (from -7.5° till 7.5°) were performed in two directions: along the tensile load direction and perpendicular to the tensile direction. Single peak fitting of diffraction patterns was carried out with the pseudo-Voigt function using the TOPAS software. The lattice strain was calculated using the following equation:

$$\varepsilon_{hkl} = \frac{d_{hkl} - d_{hkl}^0}{d_{hkl}^0} \quad (1)$$

where ε_{hkl} , d_{hkl} and d_{hkl}^0 are the lattice strain, inter-planar spacing under stress and stress-free lattice spacing of (hkl) crystallographic plane family, respectively [50].

After in situ tensile testing, the fractured samples were tomography scanned by a ZEISS Xradia 620 Versa 3D X-ray microscope to identify defects. The tomography results were stitched from the two high-resolution scans with 1.25 μm voxel resolution, which were done by 50 keV beam with a $4 \times$ magnification secondary objective lens. Each scan was covering 360° with 3000 equally spaced projections and each projection taking 12 s. The tomography, from both synchrotron and laboratory sources, was analysed by Avizo 2020.1 (Thermo Fisher Scientific). 3D median filter followed by interactive thresholding was used with the thresholding values chosen based on the Otsu's method [51].

3 Results and Discussion

In this section, we first presented the microstructural characterisation of the as-fabricated $\text{TiB}_2/\text{Al-Cu}$ composite, including porosity, grain structure, TiB_2 and Al_2Cu phase, as well as nanoprecipitation. Afterwards, the tensile mechanical properties of the alloy were presented together with the in situ diffraction and tomography analysis.

3.1 Porosity

Figure 1 shows a three-dimensional visualisation of pores in the gauge section of the as-fabricated $\text{TiB}_2/\text{Al-Cu}$ composite, which was obtained from the CT data. No crack but many

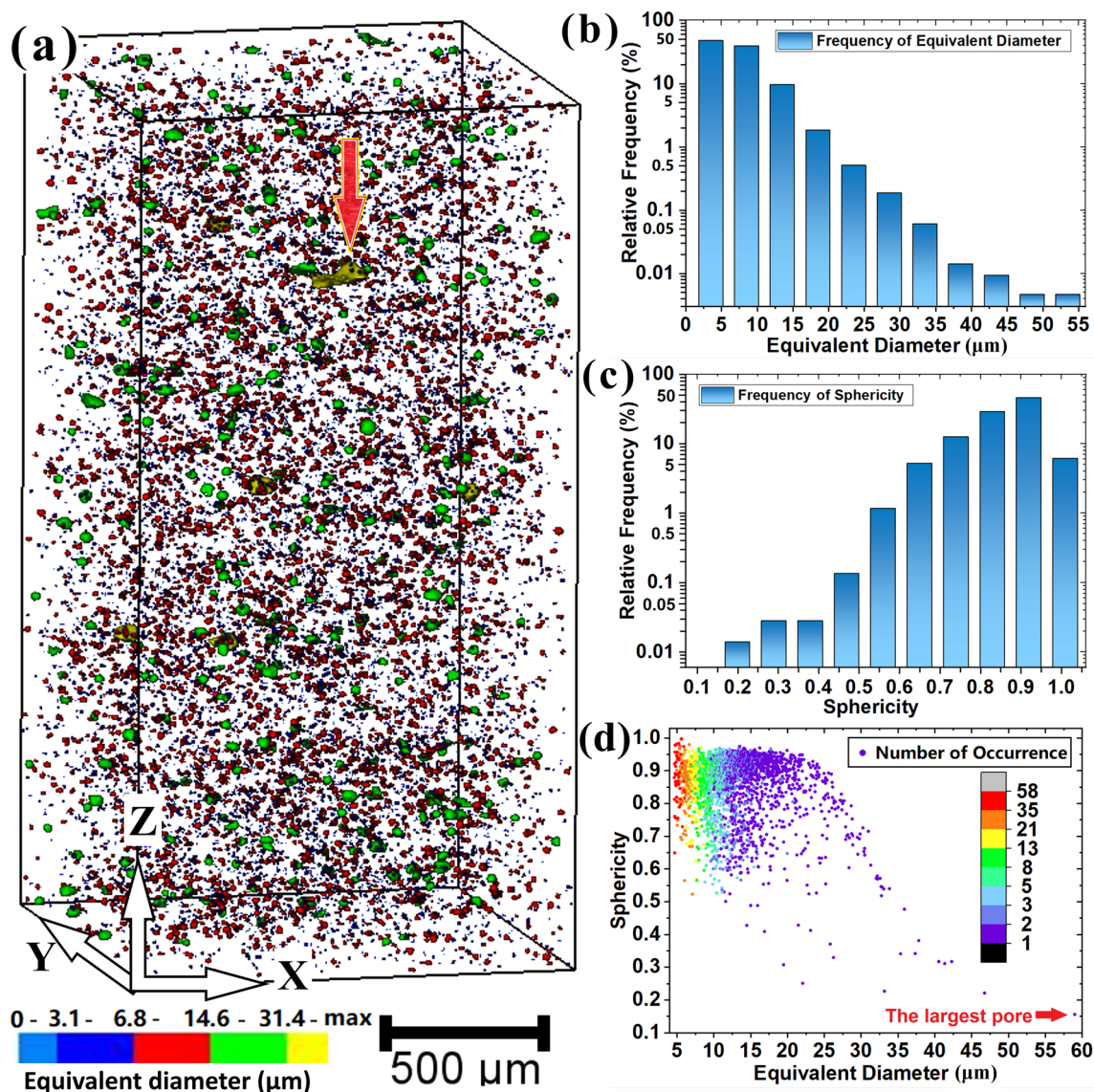


Fig. 1 X-ray tomography characterisation and analysis of the pores in the as-fabricated TiB₂/Al-Cu composite: **a** three-dimensional visualisation of pores; **b** the histogram of pores equivalent diameters shown in logarithmic scale; **c** histogram of porosity sphericity shown in logarithmic scale; and **d** sphericity versus equivalent diameter, the colour scale indicates the number of pores at certain size and sphericity. The red arrows indicate the largest pore in the section

relatively homogeneously distributed pores were observed within the sample. The pores were rendered in three different colours according to their sizes, as shown in Fig. 1a. The average equivalent diameter of the pores is $7.1 \pm 3.7 \mu\text{m}$, and the volume fraction of pores is 0.43 vol.%. Most pores within the sample are small which were rendered as red and green in Fig. 1a. Figure 1b shows the histogram of the equivalent diameter (d) of the pores. The pores with an equivalent diameter less than $3.9 \mu\text{m}$ (3 times that of resolution) were excluded, due to the noise reduction process. More than 70% of voids are smaller than $10 \mu\text{m}$, which were identified as small pores, while less than 0.03% are larger than $30 \mu\text{m}$,

which were identified as large pores. Figure 1c shows the sphericity of pores (ϵ), which was determined by Eq. 2:

$$\epsilon = 36\pi^{1/3} \cdot V_p^{2/3} \cdot A_p^{-1} \quad (2)$$

where V_p is the volume of the pores, and A_p is the surface area of the pores [52]. Both V_p and A_p were obtained from the quantification of CT data. The histogram of sphericity within the logarithmic scale is presented in Fig. 1c, showing more than 85% of pores have near spherical morphology ($\epsilon > 0.7$), and less than 0.3% of pores have lower sphericity ($\epsilon < 0.5$), which are considered as irregular shapes. In addition, there is a strong relationship between equivalent diameter and

sphericity in LPBF TiB₂/Al-Cu composite, as shown by the plot of sphericity versus diameter (Fig. 1d). The colour scale in Fig. 1d indicates the number of pores in a certain size and sphericity. It is found that the larger pores ($d > 30 \mu\text{m}$) are the least spherical, which is a lack-of-fusion defect [53, 54]. The largest pore found in the section is $58 \mu\text{m}$ diameter with 0.15 sphericity (indicated by the red arrow in Fig. 1a and d). The most of pores are small and spherical pores, which might be hydrogen gas pores formed during solidification.

3.2 Grain Structure

Typical melt pool patterns with around $150 \mu\text{m}$ in width were revealed by the EBSD band contrast map in Fig. 2a. The EBSD IPF map (Fig. 2b), along the building direction (BD or Z), reveals a distinctive fine equiaxed structure with an average size of $0.86 \pm 0.49 \mu\text{m}$. The grain size is less and a half of other LPBF Al composite prepared by mechanical powder blending, which is more than $2 \mu\text{m}$ in size [29, 36].

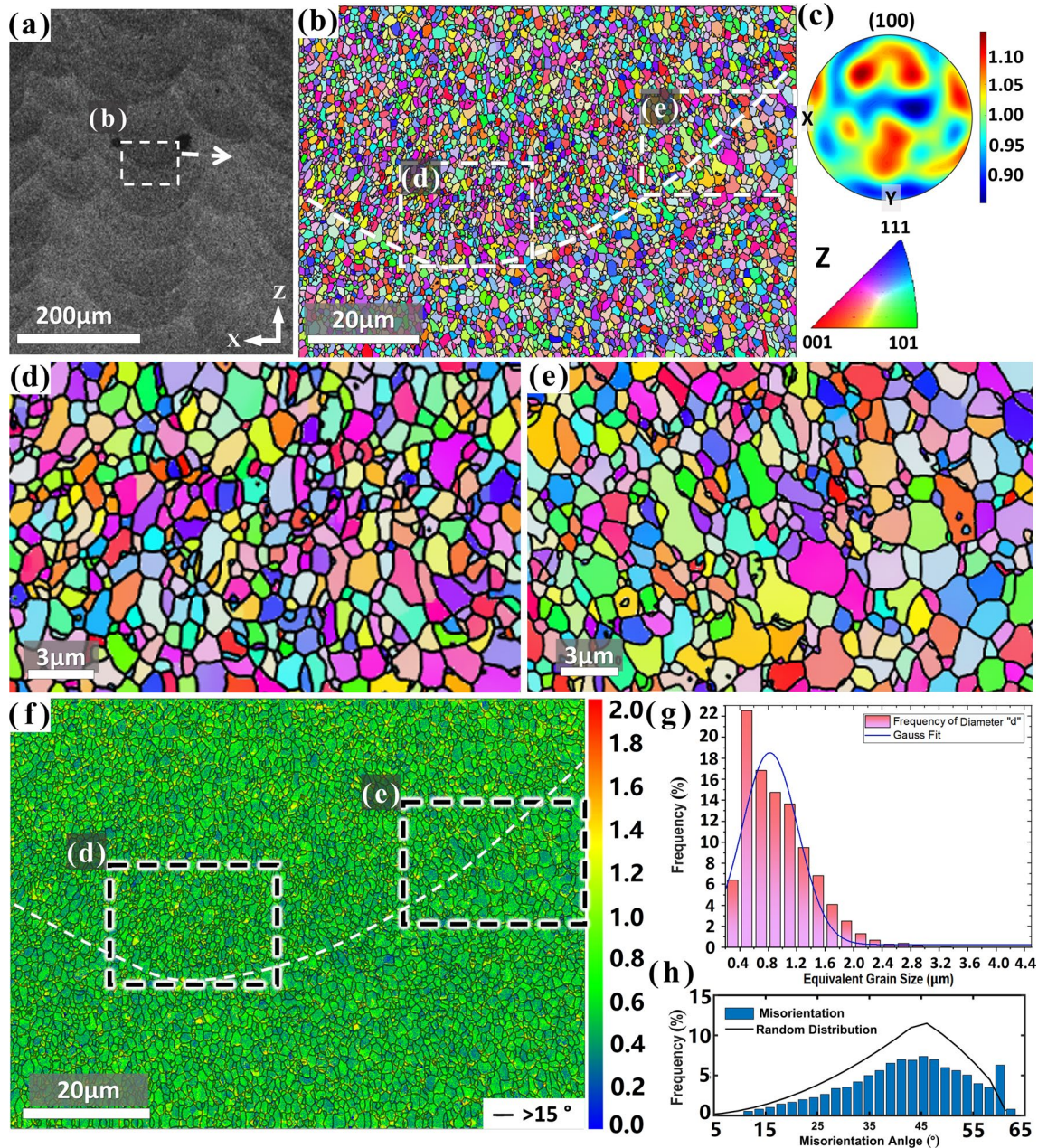


Fig. 2 EBSD map results of **a** melt pool structure in the band contrast map of as-fabricated LPBF TiB₂/Al-Cu composite; **b** IPF map, with equiaxed grains with $0.86 \mu\text{m}$ average size and weak texture, the melt pool boundary indicated by white dash line; **c** pole figure of **b**; **d** sub-set d of IPF map **b**; **e** sub-set e of IPF map **b**; **f** KAM and grain boundary map with even misorientation distribution; **g** grain size distribution calculated from IPF map **b**; and **h** misorientation distribution

Figure 2g shows the grain size distribution. Most grains are within the range between 0.3 and 1.6 μm . The decrease in grain size would improve the mechanical properties of the composite. In addition, the LPBF TiB₂/Al-Cu composite in this work shows a more homogeneous microstructure than other LPBF Al alloys and composite. The (100) pole figure (PF) in Fig. 2c has low intensity (maximum 1.1). Compared to the LPBF printed Ti-modified Al-Cu-Mg alloys, the grain size in the present work is significantly smaller (0.86 μm vs. 1.64 μm), while the maximum texture intensity is similar (1.1 vs. 1.188) [55]. Compared to LPBFed Ti-modified A205 alloys, the grain size in the present work is similar (0.86 μm vs. 0.96 μm), while the maximum texture intensity is smaller (1.1 vs. 1.36) [37]. The calculated texture J-index [56] is 1.02 which confirms the material exhibits a weak texture (where unity J-index corresponds to a random texture while a single crystal texture has infinity J-index). This is different from a typical highly textured grains microstructure found in other LPBF materials [9, 57, 58].

The area near the melt pool boundaries, between the white dashed lines in Fig. 2b, consisted of many fine grains under 1 μm as shown in Fig. 2d. Grains within the melt pool had a slightly larger size, of around 2 μm , but remained equiaxed (Fig. 2e). The relative finer grains at the melt pool boundaries indicate a higher cooling rate during solidification [28]. In addition, the grain boundary map in Fig. 2f shows the amount of low-angle grain boundaries (2 to 15°) is small (around 5%), which is also distinguished from typical LPBF grain structures and much less than the LPBFed Ti-modified Al-Cu-Mg alloys (11.3%) [59, 60]. The kernel average misorientation (KAM) map in Fig. 2f shows an even distribution of misorientations in the as-fabricated condition (max. of 2). The distribution of misorientation is shown in Fig. 2h, suggesting that the most misorientation angle is around 45° with even distribution. This is similar to the LPBFed Ti-modified Al-Cu-Mg alloys and Zr-modified Al-Cu-Mg alloys [55, 61]. The average misorientation angles around the measured point are 42.04°, which can be used to calculate the geometrically necessary dislocations (GNDs) density ρ_{GND} [62, 63]:

$$\rho_{\text{GND}} = \frac{2\theta}{u\mathbf{b}} \quad (3)$$

where θ is the average misorientation angle, u is the unit length (equivalent to the step size, 0.1 μm), and \mathbf{b} is the Burgers vector (0.286 nm for aluminium [64]). The calculated GNDs density of the as-fabricated sample is $2.94 \times 10^{12}/\text{m}^2$, which is lower than the LPBFed Al-Li alloys ($2.13 \times 10^{13}/\text{m}^2$) [62]. The low GNDs densities indicate a low residual stress level. The introduction of high melting point nanoparticles significantly improves the homogeneity of misorientation via heterogeneous nucleation. In summary, EBSD results demonstrate a distinctive microstructure in

the as-fabricated LPBF TiB₂/Al-Cu composite: fine equiaxed grains, a weak texture, a narrow range grain-size distribution, high fractions of high-angle grain boundaries, and evenly distributed misorientation. The rapid cooling nature of the AM process and high temperature gradients normally introduce directional microstructure with large and elongated grains [65]. This heterogeneous microstructure often leads to anisotropy mechanical properties of materials and becomes a challenge in AM application [66]. This study shows that pre-doping TiB₂ in Al-Cu alloys can significantly reduce the grain size, hence improve the microstructural homogeneity of LPBFed Al alloys composites.

3.3 Secondary Particles (Al₂Cu and TiB₂)

Figure 3a presents the three-dimensional rendering of a Cu-rich area in the LPBF TiB₂/Al-Cu composite, taken by FIB-SEM using backscattering contrast. The formation of this defect might be caused by the Cu-rich spatter generated during processing, and the detail is discussed in supplementary. Fine globular grains are surrounded by secondary phases (in white contrast). As shown by the zoomed-in image (Fig. 3b), the secondary phase appears to be highly connected. The 3D EDS (Fig. 3c) mapping of the same region confirmed the phase is rich in Cu; hence, they were identified as Al₂Cu according to the alloy's solidification path [67]. The Al₂Cu particles are finer than those reported in casted Al-Cu alloys [68]. The EDS point analysis shows the Cu composition in the α -Al matrix is 1.28 wt%, although the overall Cu composition in the material is around 5 wt%. The Cu dissolved in the Al matrix via solute trapping during rapid solidification [69]. Most of Cu is segregated to grain boundaries as θ -Al₂Cu precipitates.

In addition to Al₂Cu, faceted shaped particles that have slightly different contrast from the matrix were also observed, as marked by the dash lines and arrows in Fig. 3b. EDS analysis (Ti map of Fig. 3c) shows that these particles are rich in Ti; hence, they were identified as TiB₂ particles. The area fraction of TiB₂ was around 7%, as calculated from the BSE images. The typical TiB₂ morphology in Al alloys is a cuboidal or hexagonal shape, with some occasionally rod-shaped [31, 70]. The large TiB₂ particles have similar size and morphology to those observed within the powders, locating on the dendrite boundaries as shown in Fig. 4a. Figure 4b shows the TiB₂ particles are a few μm in size, comparable to the size of the grains. Some of them clustered together into a flower shape in as-fabricated samples (Figs. 3b, and 4b). One TiB₂ particle together with Al₂Cu from the 3D FIB-SEM dataset was rendered as shown in Fig. 4c and d—TiB₂ (red) and Al₂Cu (yellow). This TiB₂ particle has a rectangle pie shape with around 200 nm in thickness and 1 μm in width; hence, it looks like a rod shape

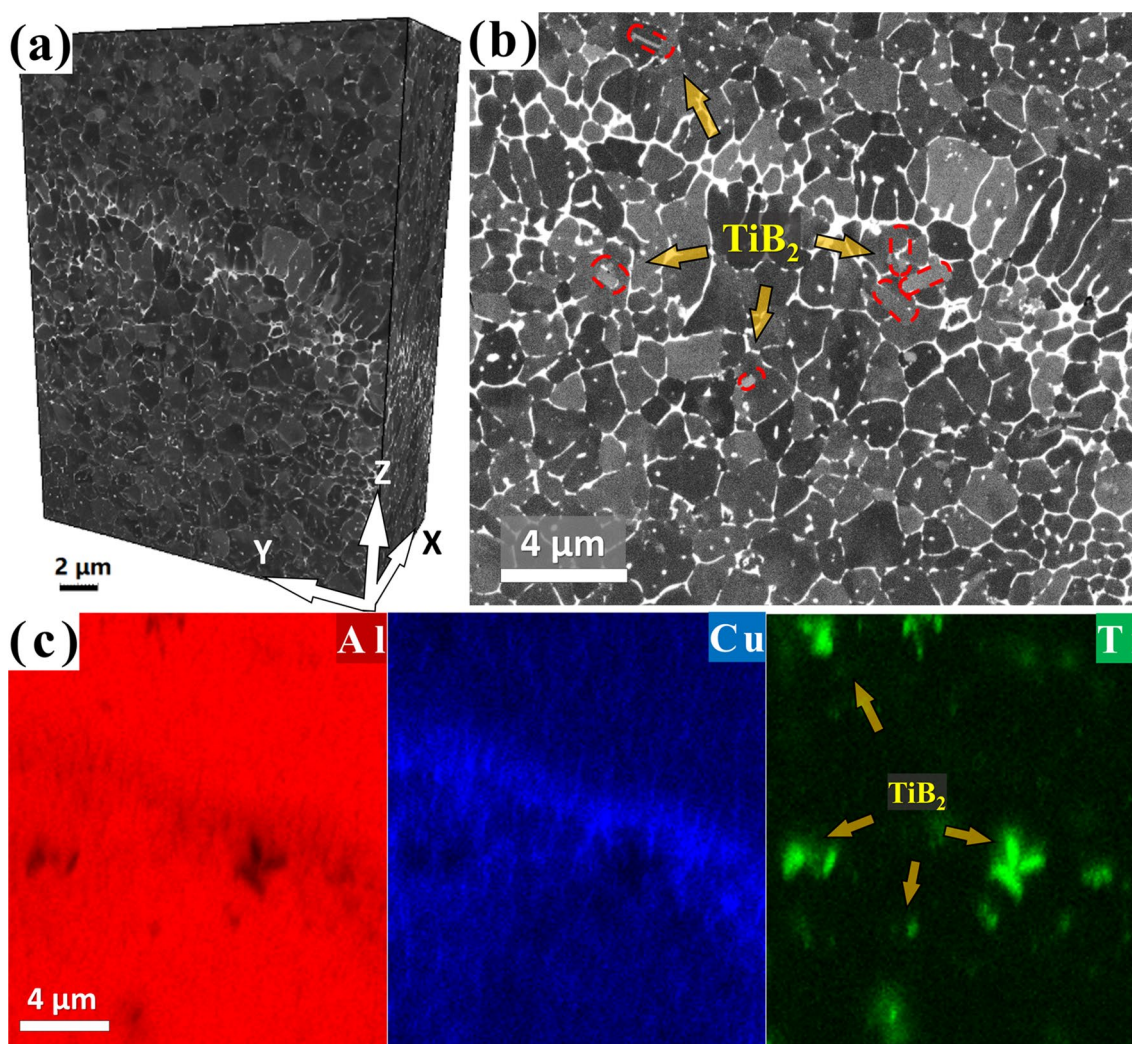


Fig. 3 Correlative electron microscopy (CEM) of LPBF $\text{TiB}_2/\text{Al-Cu}$ composite: **a** 3D reconstruction result of backscatter imaging; **b** 2D microstructure with TiB_2 indicated by yellow arrows, red dash lines; and **c** EDS map where the bright contrast area is Cu-rich, while TiB_2 clustered as a flower shape

particle from the side (Fig. 3a). The rectangle shape particle has a round edge and corner.

High-resolution scanning transmission electron microscopy (STEM) was used to further characterise the secondary particles (Fig. 5). High-angle annular dark-field images (HAADF) show both TiB_2 and Al_2Cu particles. We used EDS mapping to identify the species of the particles (Ti mapping to identify TiB_2 , and Cu mapping for Al_2Cu). Large rectangle TiB_2 particles were found with a size of around 500 nm presented at the grain boundaries. A few TiB_2 particles with a size of about 50 nm were found within the grain, as indicated by blue arrows in Fig. 5a. A cluster of small TiB_2 particles was found, located at the left top corner within the grains. The nanosized TiB_2 particles within the grain could be the main nucleation sites for primary grains during solidification. The large TiB_2 particles on the grain

boundaries might also serve as potential nucleation for multiple primary grains around its facets. Additionally, they can serve as pinning particles to restrict grain growth, which can also reduce grain size. The formation of fine grains due to heterogeneous nucleation also helps to prevent hot tearing via reducing volumetric solidification shrinkage during solidification [28, 32]. This combination of fine and large TiB_2 particles reduces the distance between nucleation sites which causes fine grain in $\text{TiB}_2/\text{Al-Cu}$ composite, comparable or slightly finer than the other Ti-modified Al alloys [55].

The Al_2Cu particles, identified by the Cu element map, are mainly presented at the grain/dendrite boundaries, or attached to the TiB_2 particles as indicated by yellow arrows in Fig. 5a. They were formed because of segregation during solidification. Higher-magnification STEM characterisation in Fig. 5b reveals elements distribution at the grain boundary

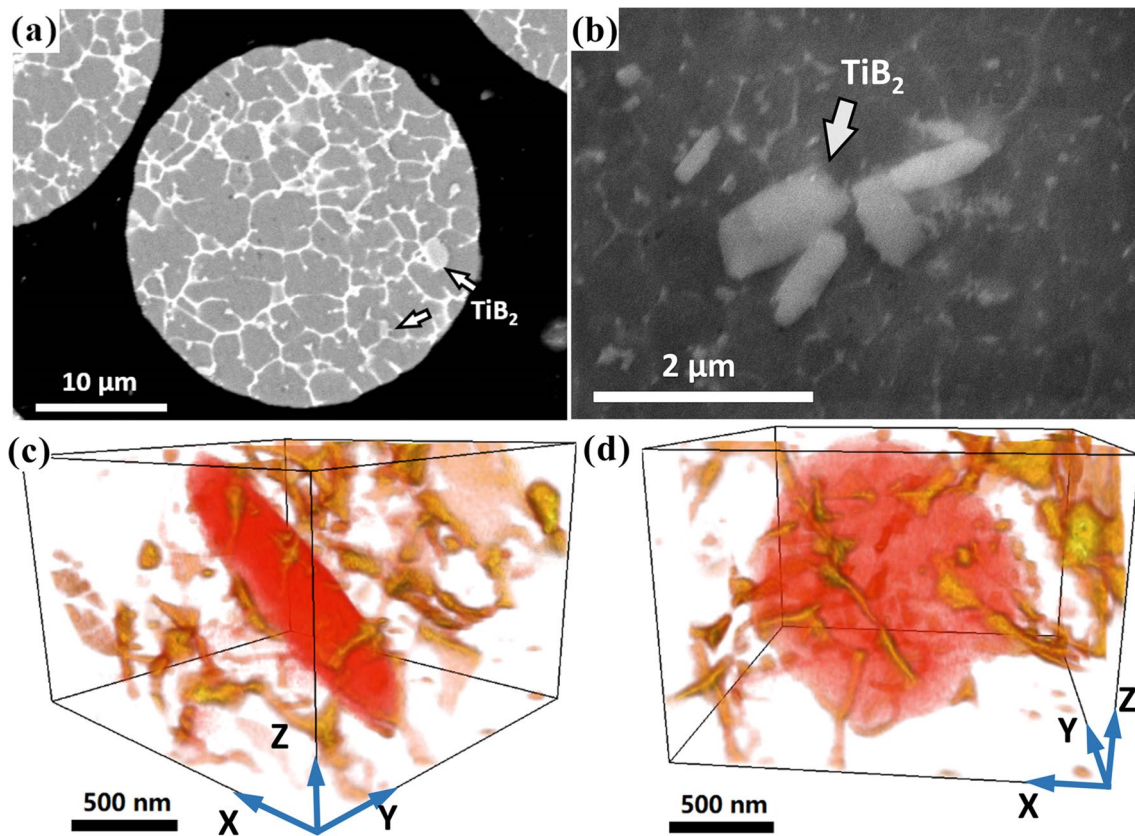


Fig. 4 SEM imaging of **a** TiB₂ particle found in powder, **b** TiB₂ particle cluster in as-fabricated composite, **c** and **d** three-dimensional reconstruction of TiB₂ (red colour) and Al₂Cu precipitates (yellow colour)

and Al₂Cu precipitates. It is found that the grain boundary is slightly enriched with Cu, Mg and Ag as shown by the white arrows in Fig. 5b. A particle-free zone was also observed along the boundaries. A triangular-shaped Al₂Cu particle is decorated within the grain trijunction. There appear to be some other particles embedded within the Al₂Cu, shown by red and blue arrows, which are Ag- and Fe-rich, respectively.

The high-resolution bright-field (BF) TEM image of a nanosized TiB₂ particle in Al matrix shows that the particles have square shape morphology, and the distance between the (0001) plane is around 3.2 Å, as shown in Fig. 6a. Interphase between TiB₂ and Al matrix was observed with a contact angle of 90° on the (0001) plane of TiB₂. The EDS results in Fig. 5a (blue arrow) show the interphase is enriched with Cu. Similar interphase in aged Al-Zn-Mg-Cu alloys reinforced with TiB₂ was reported previously [71]. The repeated cycle of laser heating and the preheated platform (150 °C, which is very close to 170 °C ageing temperature) in LPBF provided a higher temperature in situ ageing environment for the printed TiB₂/Al-Cu composite, thus allowing interphase to be formed, which might reduce the mismatch of the TiB₂/Al interface [71, 72]. This semi-coherent TiB₂/Al interface is considered beneficial to the heterogeneous precipitation,

which reduces nucleation energy barrier and diffusion paths for transporting solute atoms and vacancies during ageing [73].

3.4 Nano-precipitates

It is well known that the Guinier–Preston (GP) zone in Al alloys is a metastable solute-rich cluster and develops to θ or S phase during the following ageing treatment [74, 75]. The high-angle annular dark-field image (HADF) image in Fig. 7a shows bright nanosize particles homogeneously distributed within the α-Al matrix. A higher-magnification TEM investigation in Fig. 7b shows particles are below 10 nm size corresponding to the GP zone [76]. The fast Fourier transformation (FFT) pattern and the corresponding inverse FFT image of area 1 (marked square area) in Fig. 7a illustrate diffuse streaks along (111) planes of α-Al direction, indicating that the GP zone forms on these planes. The formation of the GP zone in the as-fabrication sample could be due to the 150 °C platform preheat which introduced the ageing effect during manufacturing, as this temperature is very close to the ageing temperature of Al-Cu alloys (around 170 °C). However, it is difficult to identify

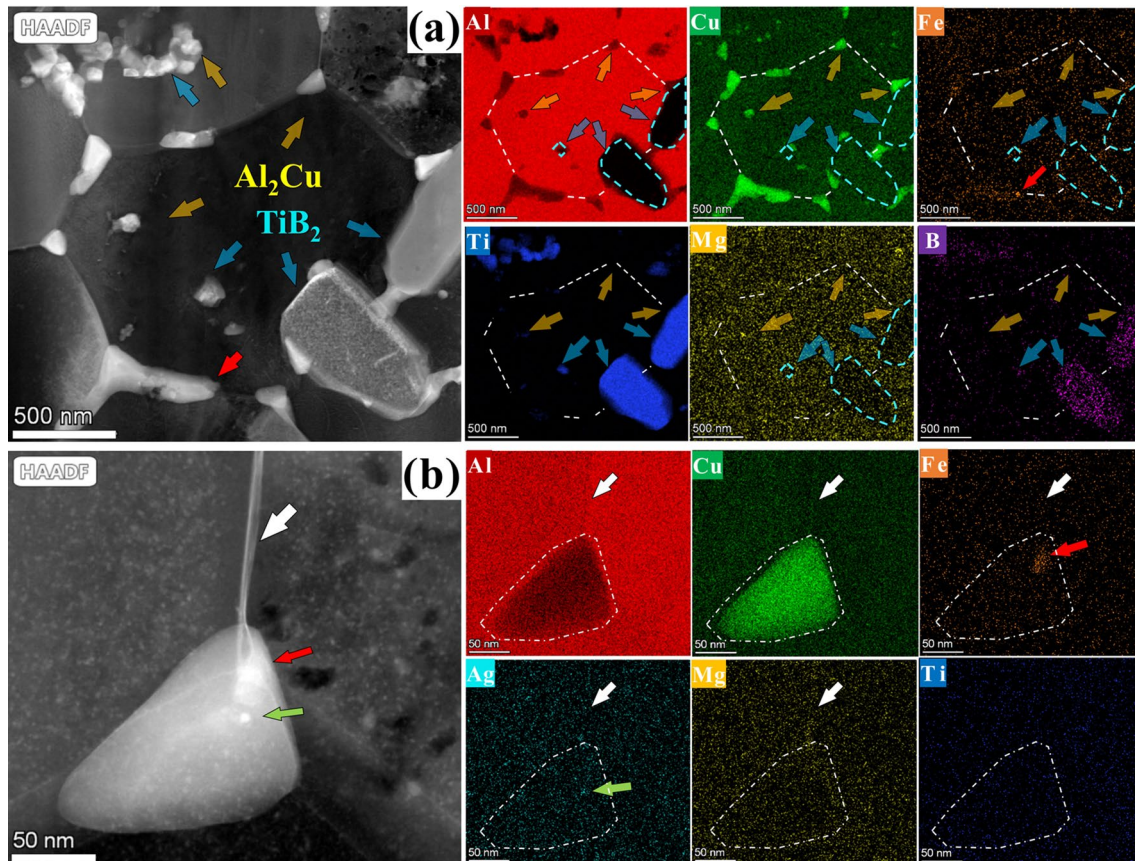


Fig. 5 STEM characterisation of LPBFed $\text{TiB}_2/\text{Al-Cu}$ composite: **a** fine TiB_2 particles (around 50 nm) in $\alpha\text{-Al}$ grain, while large TiB_2 particles around 500 nm size at grain boundary (indicated by blue arrows), and Al_2Cu precipitates (indicated by yellow arrows) at the grain boundary (indicated by white dash lines); **b** Al_2Cu precipitating particles around 150 nm and grain boundary (indicated by white arrows), EDS mapping at grain boundary showing slightly Cu-, Ag- and Mg-rich, and the fine particles in Al_2Cu precipitate is Ag- and Fe-rich (indicated by red and blue arrows, respectively)

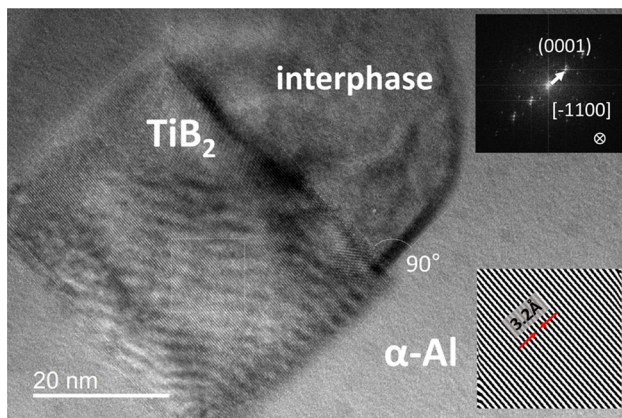


Fig. 6 TEM bright-field image on fine TiB_2 particles in $\alpha\text{-Al}$ matrix, with d_{001} plane distance of 3.2 Å

the chemical composition and morphology of the GP zone, advanced characterisation, such as atom probe tomography and aberration-corrected TEM would be required. Further

TEM characterisation will be carried out in a future study, especially as a function of post-process heat treatments to maximise the strength of the alloy.

3.5 Mechanical Properties

The stress–strain curves of the as-fabricated LPBF $\text{TiB}_2/\text{Al-Cu}$ composite from standard tensile tests are shown in Fig. 8, together with the in situ testing result. The average yield strength and ultimate tensile strength (UTS) of three standard tensile tests were 316.9 ± 7.3 MPa and 403.2 ± 6.9 MPa, respectively. The total elongation was $10.2\% \pm 0.5\%$, and the elastic modulus was 71.35 GPa. The standard tensile tests show similar mechanical properties to the in situ tests despite the different sample morphology. Figure 8b shows the comparison of yield strength and total elongation between LPBF fabricated $\text{TiB}_2/\text{Al-Cu}$ composite and other LPBF Al alloys and composites. The LPBF $\text{TiB}_2/\text{Al-Cu}$ composite has similar yield strength to the LPBF $\text{TiB}_2/\text{Al-Cu-Mg-Si}$ composite [36]

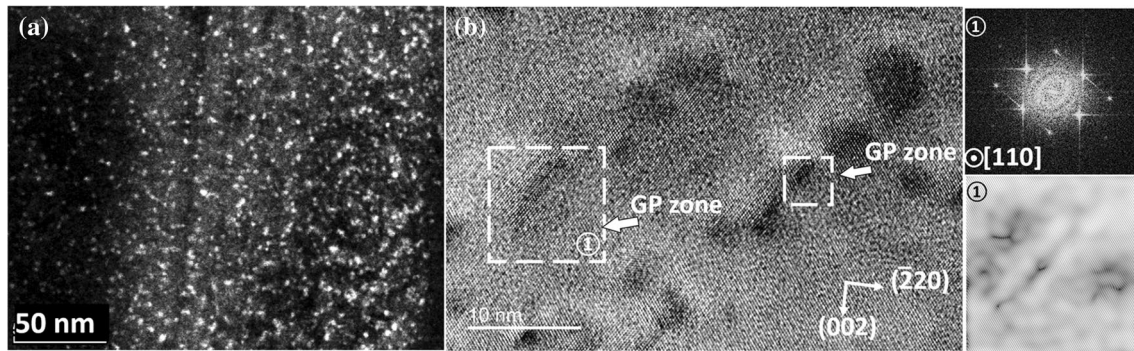


Fig. 7 STEM characterisation reveals nanosize particles within the Al matrix: **a** HADDF image with bright particles of a few nm in Al matrix and **b** higher-magnification image and the diffraction pattern of the matrix nanoparticles and GP zone

and Ti-modified Al-Cu alloys [37, 55], but higher than the TiB₂ pre-doped A205 alloys (269 MPa) [37].

3.5.1 Strengthening Mechanism

The yield strength of Al alloys can be calculated by the following equation [77]:

$$\sigma_y = \sigma'_0 + \sigma_{ss} + \sigma_{gb} + \sigma_{dis} + \sigma_p \quad (4)$$

where σ'_0 is the yield stress (σ_y) of pure Al (about 50 MPa) [78], σ_{ss} is the solid solution strength for Cu in Al, which is 7 MPa/wt% [77, 79]. According to the EDS analysis, the solid solution of Cu in Al matrix is 1.3 wt%; therefore, the σ_{ss} is 9.1 MPa. Although there are other elements like Mg, Fe, Ag and Si in the materials, the percentage of these elements is very low. Therefore, they were not included in this calculation. The σ_{gb} is grain boundary strength, σ_{dis} is dislocation strength, and σ_p is particle dispersion strength.

The contribution of grain boundaries (σ_{gb}) can be calculated by the Hall–Petch relation [80]:

$$\sigma_{gb} = k_1 D_{GB}^{-1/2} \quad (5)$$

where D_{GB} is the grain size. k is a constant, which was reported as 0.08 MPa·m^{1/2} [77]. Accordingly, the yield strength caused by the ultra-fine grain is 86.3 MPa. The results suggest the refinement of grain size provided higher strength compared to the LPBF TiB₂/Al-Cu composite manufactured via mechanical blending (79.6 MPa for 2.5 μ m average grain size [36]).

The strength contribution from dislocation (σ_{dis}) can be calculated with the Taylor equation:

$$\sigma_{dis} = M\alpha Gb\rho^{1/2} \quad (6)$$

where M is the Taylor factor (~ 3 for randomly oriented fcc polycrystals) [64, 81]. α is a constant, which is $\sim 1/3$ in aluminium [82]. G is the shear modulus of Al (28 GPa), and b

is the Burgers vector of Al (0.286 nm). ρ is the dislocation density, which is calculated from EBSD results. Therefore, the contribution to strength from dislocation was estimated to be about 13.7 MPa.

The microscopy analysis shows a few different particles with various morphology, size and composition in the LPBFed TiB₂/Al-Cu composite, including Al₂Cu at grain boundaries, micrometer and nanometer size TiB₂, and GP zones. It is difficult to directly calculate the strengthening contribution of each particle using Orowan mechanism, but the total contribution to strength from these particles (σ_p) can be calculated using experimental results and Eq. 4:

$$\sigma_p = \sigma_y - (\sigma'_0 + \sigma_{ss} + \sigma_{gb} + \sigma_{dis}) \quad (7)$$

The calculated yield strength apart from σ_p was 159.1 MPa. Hence, the estimated total contribution to strength from Al₂Cu, TiB₂, GP-zones and a small number of other elements (including Ag, Fe and Mg) was 157.8 MPa.

As shown in Fig. 8a, the stress–strain curve of in situ tensile testing is very close to that of the standard test. To record diffraction and tomography measurements, the tensile specimen was held at different displacement levels after yielding. The stress values dropped during the holding period due to stress relaxation.

3.5.2 In Situ Diffraction during Tensile Loading

In situ high-energy X-ray diffraction examination was performed to provide atomic-level strains to help understand the deformation mechanisms of the as-fabricated LPBF TiB₂/Al-Cu composite. Figure 9a shows the diffraction patterns of the sample, where the diffraction peaks of α -Al matrix, TiB₂ and Al₂Cu phases were observed and identified.

Figure 9b shows the lattice strain versus stress in 0° (tensile loading direction (LD), parallel to build direction (BD)) and 90° (transverse) directions. The lattice strain linearly increased with increasing stress during elastic deformation.

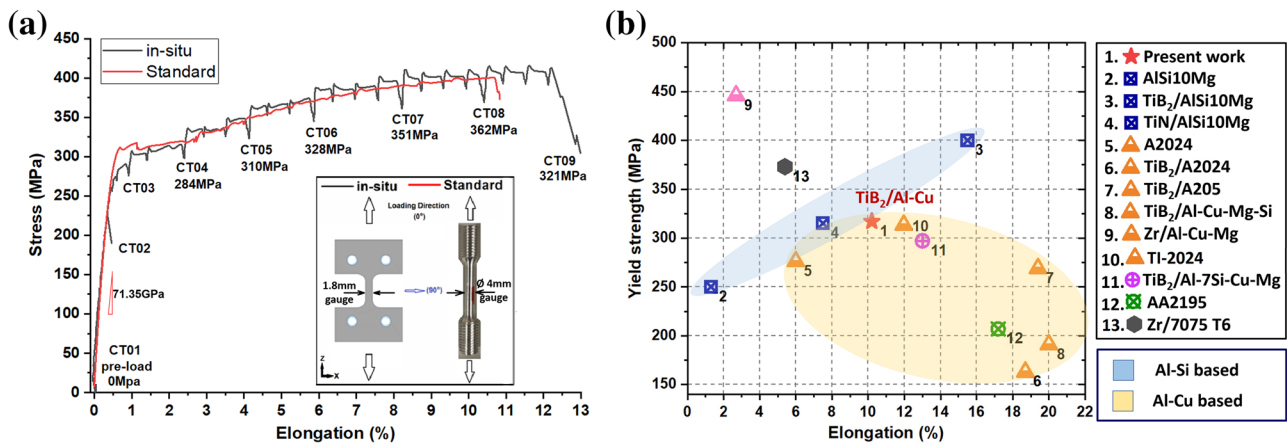


Fig. 8 Strength–strain curves of as-fabricated LPBF $\text{TiB}_2/\text{Al-Cu}$ composite samples under standard tensile and in situ tensile tests

The Young's modulus, as well as Poisson's ratio of the as-fabricated $\text{TiB}_2/\text{Al-Cu}$ composite in each crystallographic orientation, was calculated by linearly fitting the elastic deformation stage as listed in Table 1. The variation between different grain families is small (around 6%). It is found that the (111) and (200) grains exhibit the lowest and greatest tensile elastic modulus, respectively. This is similar to other face-centred cubic materials [83]. However, (220) grain family shows the highest Young's modulus under compression. The Poisson's ratios are around 0.3 in most of the grain families apart from (220), which is 0.12.

A drop of lattice strain after the elastic stage, parallel to the loading direction (LD), was found in all lattice planes. The softer matrix $\alpha\text{-Al}$ grains are easier to deform than the more rigid AlCu_2 and TiB_2 particles, which leads to plastic stress partitioning [84, 85]. The transition period starts from yielding onset until reaching yield strength, and the nonlinear stress–strain relationship indicates the load transfers from 'softer' grain families, e.g. (220), to 'harder' grain

Table 1 Orientation-dependent Young's modulus and Poisson's ratio of the as-fabricated $\text{TiB}_2/\text{Al-Cu}$ composite

Lattice direction	(111)	(200)	(220)	(311)
Tensile E_0 (GPa)	86.6	81.0	84.9	81.8
Compressive E_{90} (GPa)	−280.9	−220.8	−714.3	−245.7
Poisson's ratio ν	0.31	0.37	0.12	0.33

families, e.g. (200). The lattice strain in (200) started the reduction first at 260 MPa, followed by (311) and (220) grains. They have a similar amount of strain reduction until reaching 0.2% yield strength at 316 MPa (indicated by the yellow dash line). However, the lattice strain of (111) grains remains at the same level during yielding. This is because the distance between lattice planes in (111) direction is the smallest, while the distance in (200) direction is the largest. The strain partitioning starts at the loosest lattice planes where the resistance is the smallest. At the end

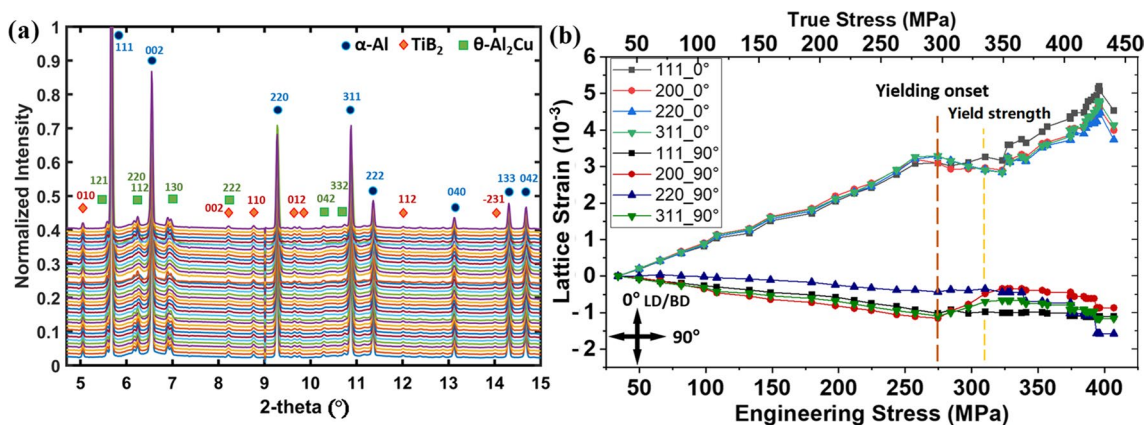


Fig. 9 Diffraction of LPBF $\text{TiB}_2/\text{Al-Cu}$ composite during tensile loading: **a** diffraction peaks and presents phases and **b** lattice strain versus stress including elastic deformation stage, transition period (260 MPa–320 MPa), and stress redistribution during the plastic deformation stage

of the transition period, a clear step of strain increasing was found in all crystal directions after yield strength, which indicates the start of plastic deformation. Afterwards, the lattice strain responds linearly to the applied stress again as the sequence of $(220) = (311) < (200) < (111)$. The lattice strain in (111) grain family is significantly larger than the other directions during plastic deformation, as the slip plane for lowest energy dislocation is [86] close packed plane.

3.5.3 Tomography Analysis

X-ray CT scans during in situ tensile testing at 0 MPa, 351 MPa, 369 MPa, and 321 MPa (after sample necking) show the development of pores and cracks (see Fig. 10). The crack initiates from an irregular pore within the as-fabricated sample (marked by the yellow arrow). This pore was extracted out from the volume and is shown in Fig. 10e-g. By comparing the CT result after loading (Fig. 10) and statistical results before the loading (Fig. 1d), it was found that the initial pore was irregular (0.15 sphericity) and the largest (58 μm equivalent diameter) within the sample volume,

which might be a lack-of-fusion pore. It increased from 58 μm to 400 μm during loading as shown in Fig. 10a-d. Two small irregular pores of around 10 μm , about 400 μm away from the largest pore at the same horizontal plane, were also expanded and coalesced with the largest pore after 351 MPa, as indicated by the orange arrow in Fig. 10b. The largest pores propagated to a V-shape crack after reaching the ultimate strength.

The statistical quantification of porosity is shown in Fig. 11. Both volume fraction and the size of the maximum pore within the materials gradually increased from 0.45% and 59 μm to 0.68% and 88 μm , respectively, during the plastic deformation stage (below 362 MPa). The size of the maximum pore then proliferates during further loading and reached around 400 μm at 369 MPa (near the ultimate tensile strength). The number of pores and the average diameter, however, remain at the same level during plastic deformation. Together with the 3D results shown in Fig. 10, it can be concluded that it was the largest lack of fusion defect that developed into cracks during tensile loading.

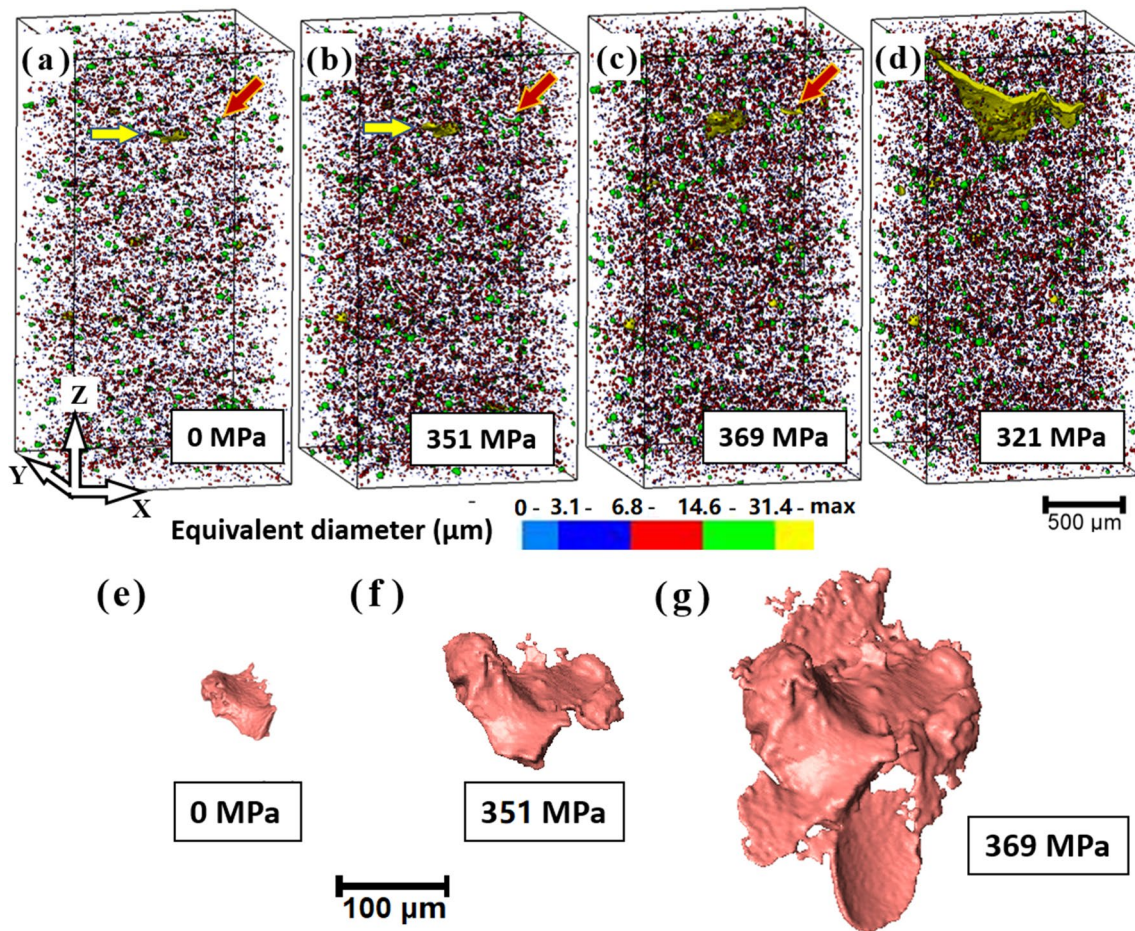


Fig. 10 In situ μCT results of porosity during tensile loading a-d, and crack development during tensile loading e-g

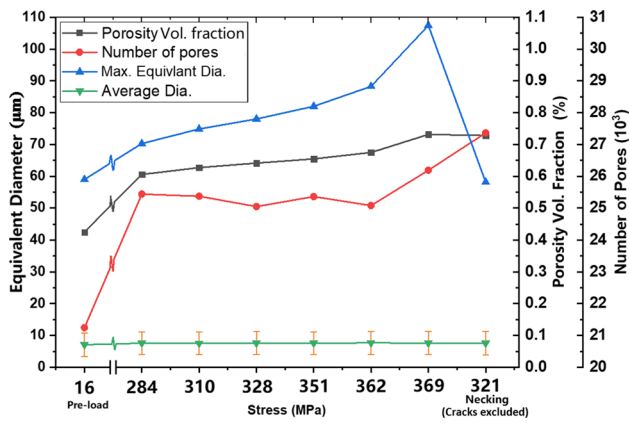


Fig. 11 Variation of porosity, number of pores, maximum pore diameter and average pore diameter during tensile testing

3.5.4 Fracture Surface

The fractured surface of in situ sample and standard mechanical test samples were similar. The three-dimensional visualisation of the fractured surface is shown in Fig. 12a, and the area of the initial pores is indicated by the black dash box. This initial pore is consistent with the largest irregular porosity in this area, revealed by CT visualisation before loading. The porosity grew uniformly across all directions during tensile loading, before developing into a V-shaped

crack before breaking. The fractography in Fig. 12c shows a few spherical dimples within the centre-right area (crack nucleation region) of the fractured surface (indicated by the white box in Fig. 12b). Higher-magnification SEM images show that there are spherical particles of around 10 µm size within the dimples, confirming the pore that opened into the crack is a lack-of-fusion defect. The brittle fracture around the crack nucleation area is shown in Fig. 12d, which indicates the fracture transformed from ductile to brittle during loading. Further high-magnification image in Fig. 12e reveals intergranular fracture near the crack initiation region, which indicates that cracks propagate along the grain boundaries after yielding. Further away, the brittle fracture area with a relatively smooth surface was observed, suggests the cracks propagate quickly through the slip plane, and shows shear dominated failure [87]. Figure 12f shows a defect, within which particles of around 4 µm size are observed. This defect is around 400 µm away from the crack initiation region. This is associated with the secondary crack developed from small irregular pores after 351 MPa, indicated by the orange arrow in Fig. 10c. The fractography investigation combined with in situ µCT results suggests the fracture was opened from a lack-of-fusion defect (red circle in Fig. 12b) via grain boundary cracking before 328 MPa. The fracture then transformed from ductile (area indicated by the yellow line in Fig. 12b) to brittle fractures after 369 MPa (green lines in Fig. 12b), leading to final failure.

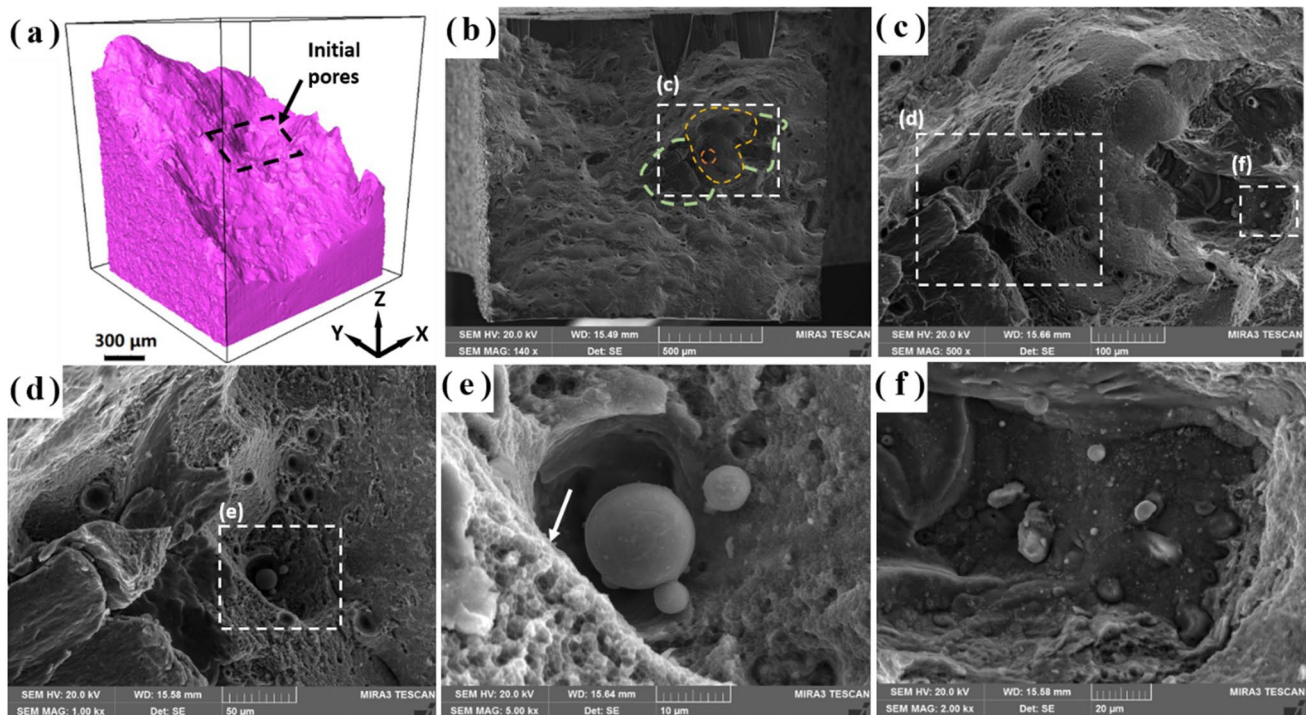


Fig. 12 Fractography of the in situ test samples after failure: **a** 3D volume rendering of the CT scan of the fractured specimen; **b–f** secondary electron images: **b** a large region showing relative smooth fracture surface with the crack initiation region, indicated by the white box; **c** the crack initiation region with some particles and smooth surface; **d** a zoomed-in image of box d in **c**; **e** a further zoomed-in image of box e in **d**; **f** a zoomed-in image of box f in **c**

4 Conclusions

This study fabricated TiB₂/Al-Cu composite by LPBF, using Al-Cu powders pre-doped with sub-micrometre TiB₂ particles. Synchrotron X-ray tomography, 3D SEM and (S) TEM were also used to study the defects and multi-scale microstructures of the TiB₂/Al-Cu composite. In situ synchrotron X-ray measurements including tomography and diffraction during tensile loading were used to investigate deformation and fracture mechanisms.

1. The printed alloy is crack-free, but many pores were found. The porosity was 0.43 vol.%, and most of the pores were small in globular morphology with an average equivalent diameter of 7.1 μm. A few large ones (equivalent diameter > 30 μm) were in irregular shapes.
2. Ultra-fine equiaxed grains with 0.86 μm average grain size were introduced by the combined effects of rapid solidification and heterogeneous nucleation on the doped nanosize TiB₂ particles. The calculations showed TiB₂/Al-Cu composite has fine grains, weak texture, low GNDs density and homogeneous misorientation distribution.
3. Nanometre sized TiB₂ particles (around 40 nm) were found within the grains, acting as heterogeneous nucleation sites. Micrometre sized TiB₂ (0.5–2 μm) particles were found located along the grain boundaries, which could serve as both nucleation sites and pinning particles for growth. Some TiB₂ were clustered together. Interphase was found between the matrix and TiB₂.
4. The tensile strength of the as-printed composite reached 403 MPa with total elongation of 10%. Orientation-dependent Young's modulus and Poisson's ratio of TiB₂/Al-Cu alloy were determined by in situ X-ray diffraction.
5. The contributions of Cu solid solution, dislocations, grain boundaries, and particles to the yield strength were calculated. The particles and grain boundaries strengthening contributed to the major part of the yield strength.
6. In situ X-ray tomography shows that during tensile loading, the fracture initiated from the biggest lack-of-fusion pore and grew alongside the slip plane into a large V-shaped crack, leading to the fracture of the specimen.

Supplementary Information The online version contains supplementary material available at <https://doi.org/10.1007/s40195-021-01317-y>.

Acknowledgements The authors acknowledge the support of the Diamond Light Source for providing the beamtime (MG22506) at the I12 beamline. Biao Cai appreciates the support from the Royal Society International Exchange Grant (IEC\NSFC\191319) and Research Grant (RGS\202122). The authors thank Prof. Yu-Lung Chiu and Dr. Minshi Wang, who helped with microscopy characterisation.

Declarations

Conflict of interest The authors state that there are no conflicts of interest to disclose.

Open Access This article is licensed under a Creative Commons Attribution 4.0 International License, which permits use, sharing, adaptation, distribution and reproduction in any medium or format, as long as you give appropriate credit to the original author(s) and the source, provide a link to the Creative Commons licence, and indicate if changes were made. The images or other third party material in this article are included in the article's Creative Commons licence, unless indicated otherwise in a credit line to the material. If material is not included in the article's Creative Commons licence and your intended use is not permitted by statutory regulation or exceeds the permitted use, you will need to obtain permission directly from the copyright holder. To view a copy of this licence, visit <http://creativecommons.org/licenses/by/4.0/>.

References

- [1] X. Wu, *Mater. Sci. Technol.* **23**, 10 (2007)
- [2] W.E. Frazier, *J. Mater. Eng. Perform.* **23**, 1917 (2014)
- [3] S.H. Huang, P. Liu, A. Mokasdar, L. Hou, *Int. J. Adv. Manuf. Technol.* **67**, 1191 (2013)
- [4] T. Hanemann, L.N. Carter, M. Habschied, N.J.E. Adkins, M.M. Attallah, M. Heilmaier, *J. Alloys Compd.* **795**, 8 (2019)
- [5] J.C. Hastie, M.E. Kartal, L.N. Carter, M.M. Attallah, D.M. Mulvihill, *Mater. Charact.* **163**, 110225 (2020)
- [6] M. Lutter-Günther, M. Bröker, T. Mayer, S. Lizak, C. Seidel, G. Reinhart, *Procedia CIRP* **74**, 33 (2018)
- [7] Y. Shi, P. Rometsch, K. Yang, F. Palm, X. Wu, *Mater. Lett.* **196**, 347 (2017)
- [8] K. Schmidtke, F. Palm, A. Hawkins, C. Emmelmann, *Phys. Procedia* **12**, 369 (2011)
- [9] A. Shyam, A. Plotkowski, S. Bahl, K. Sisco, L.F. Allard, Y. Yang, J.A. Haynes, R.R. Dehoff, *Materialia* **12**, 100758 (2020)
- [10] Q. Jia, F. Zhang, P. Rometsch, J. Li, J. Mata, M. Weyland, L. Bourgeois, M. Sui, X. Wu, *Acta Mater.* **193**, 239 (2020)
- [11] R. Li, M. Wang, Z. Li, P. Cao, T. Yuan, H. Zhu, *Acta Mater.* **193**, 83 (2020)
- [12] H. Zhang, D. Gu, J. Yang, D. Dai, T. Zhao, C. Hong, A. Gasser, R. Poprawe, *Addit. Manuf.* **23**, 1 (2018)
- [13] C. Brice, R. Shenoy, M. Kral, K. Buchannan, *Mater. Sci. Eng. A* **648**, 9 (2015)
- [14] H. Gu, S. Li, M. Pavier, M.M. Attallah, C. Paraskevoulakos, A. Shterenlikht, *Int. J. Solids Struct.* **180–181**, 147 (2019)
- [15] L. Zhou, F. Gao, G.S. Peng, N. Alba-Baena, *J. Alloys Compd.* **689**, 401 (2016)
- [16] X. Wang, A. Jha, R. Brydson, *Mater. Sci. Eng. A* **364**, 339 (2004)
- [17] D. Gu, Y. Yang, L. Xi, J. Yang, M. Xia, *Opt. Laser Technol.* **119**, 105600 (2019)
- [18] I. Polmear, D. StJohn, J.-F. Nie, M. Qian, *Light Alloys*, 5th edn. (Butterworth-Heinemann, Boston, 2017), pp. 31–107
- [19] P. Kürsteiner, P. Bajaj, A. Gupta, M.B. Wilms, A. Weisheit, X. Li, C. Leinenbach, B. Gault, E.A. Jäggle, D. Raabe, *Addit. Manuf.* **32**, 100910 (2020)
- [20] D.A. Ramirez, L.E. Murr, E. Martinez, D.H. Hernandez, J.L. Martinez, B.I. Machado, F. Medina, P. Frigola, R.B. Wicker, *Acta Mater.* **59**, 4088 (2011)
- [21] C. Weingarten, D. Buchbinder, N. Pirch, W. Meiners, K. Wissenbach, R. Poprawe, *J. Mater. Process. Technol.* **221**, 112 (2015)
- [22] L.N. Carter, C. Martin, P.J. Withers, M.M. Attallah, *J. Alloys Compd.* **615**, 9 (2014)

- [23] R. Singh, A. Gupta, O. Tripathi, S. Srivastava, B. Singh, A. Awasthi, S.K. Rajput, P. Sonia, P. Singhal, K.K. Saxena, *Mater. Today: Proceedings* **26**, 3058 (2020)
- [24] J.S. Zuback, P. Moradifar, Z. Khayat, N. Alem, T.A. Palmer, *J. Alloys Compd.* **798**, 446 (2019)
- [25] P. Bale, Dissertation, The University of Birmingham, (2011)
- [26] L. Xi, S. Guo, D. Gu, M. Guo, K. Lin, *J. Alloys Compd.* **819**, 152980 (2020)
- [27] C. Gao, W. Wu, J. Shi, Z. Xiao, A.H. Akbarzadeh, *Addit. Manuf.* **34**, 101378 (2020)
- [28] J.H. Martin, B.D. Yahata, J.M. Hundley, J.A. Mayer, T.A. Schaefer, T.M. Pollock, *Nature* **549**, 365 (2017)
- [29] L. Xi, P. Wang, K.G. Prashanth, H. Li, H.V. Prykhodko, S. Scudino, I. Kaban, *J. Alloys Compd.* **786**, 551 (2019)
- [30] M. Easton, D. StJohn, *Metall. Mater. Trans. A* **30**, 1613 (1999)
- [31] S. Mozammil, J. Karloopia, R. Verma, P.K. Jha, *J. Alloys Compd.* **793**, 454 (2019)
- [32] M. Sokoluk, C. Cao, S. Pan, X. Li, *Nat. Commun.* **10**, 98 (2019)
- [33] B. Gwalani, M. Olszta, S. Varma, L. Li, A. Soulami, E. Kautz, S. Pathak, A. Rohatgi, P.V. Sushko, S. Mathaudhu, C.A. Powell, A. Devaraj, *Commun. Mater.* **1**, 85 (2020)
- [34] K. Geng, Y. Yang, S. Li, R.D.K. Misra, Q. Zhu, *Addit. Manuf.* **32**, 101012 (2020)
- [35] Q. Tan, J. Zhang, Q. Sun, Z. Fan, G. Li, Y. Yin, Y. Liu, M.X. Zhang, *Acta Mater.* **196**, 1 (2020)
- [36] P. Wang, C. Gammer, F. Brenne, T. Niendorf, J. Eckert, S. Scudino, *Compos. B Eng.* **147**, 162 (2018)
- [37] M.H. Ghoncheh, M. Sanjari, A.S. Zoeram, E. Cyr, B.S. Amirkhiz, A. Lloyd, M. Haghshenas, M. Mohammadi, *Addit. Manuf.* **37**, 101724 (2021)
- [38] C. Li, X. Liu, G. Zhang, *Mater. Sci. Eng. A* **497**, 432 (2008)
- [39] A. du Plessis, *Addit. Manuf.* **30**, 100871 (2019)
- [40] C. Puncreobutr, P.D. Lee, R.W. Hamilton, B. Cai, T. Connolley, *Metall. Mater. Trans. A* **44**, 5389 (2013)
- [41] A. International Standard Test Methods for Tension Testing of Metallic Materials (West Conshohocken, PA) (2013)
- [42] F. Bachmann, R. Hielscher, H. Schaeben, *Solid State Phenom.* **160**, 63 (2010)
- [43] M. Drakopoulos, T. Connolley, C. Reinhard, R. Atwood, O. Magdysyuk, N. Vo, M. Hart, L. Connor, B. Humphreys, G. Howell, S. Davies, T. Hill, G. Wilkin, U. Pedersen, A. Foster, N. De Maio, M. Basham, F. Yuan, K. Wanelik, *J. Synchrotron Radiat.* **22**, 828 (2015)
- [44] N. Wadson, M. Basham, Savu: A Python-based, MPI Framework for Simultaneous Processing of Multiple, N-dimensional, Large Tomography Datasets (2016), <https://arxiv.org/abs/1610.08015>, Submitted on 24 Oct 2016
- [45] W. van Aarle, W.J. Palenstijn, J. Cant, E. Janssens, F. Bleichrodt, A. Dabravolski, J. De Beenhouwer, K. Joost Batenburg, J. Sijbers, *Opt. Express* **24**, 25129 (2016)
- [46] G.N. Ramachandran, A.V. Lakshminarayanan, *Proc. Natl. Acad. Sci. U.S.A.* **68**, 2236 (1971)
- [47] M. Basham, J. Filik, M.T. Wharmby, P.C.Y. Chang, B. El Kassaby, M. Gerring, J. Aishima, K. Levik, B.C.A. Pulford, I. Sikharulidze, D. Sneddon, M. Webber, S.S. Dhesi, F. Maccherozzi, O. Svensson, S. Brockhauser, G. N ray, A.W. Ashton, *J. Synchrotron Radiat.* **22**, 853 (2015)
- [48] J. Filik, A.W. Ashton, P.C.Y. Chang, P.A. Chater, S.J. Day, M. Drakopoulos, M.W. Gerring, M.L. Hart, O.V. Magdysyuk, S. Michalik, A. Smith, C.C. Tang, N.J. Terrill, M.T. Wharmby, H. Wilhelm, *J. Appl. Crystallogr.* **50**, 959 (2017)
- [49] M.L. Hart, M. Drakopoulos, C. Reinhard, T. Connolley, *J. Appl. Crystallogr.* **46**, 1249 (2013)
- [50] Y. Wang, B. Liu, K. Yan, M. Wang, S. Kabra, Y.L. Chiu, D. Dye, P.D. Lee, Y. Liu, B. Cai, *Acta Mater.* **154**, 79 (2018)
- [51] R.F. Moghaddam, M. Cheriet, *Pattern Recognit.* **45**, 2419 (2012)
- [52] H. Wadell, *J. Geol.* **43**, 250 (1935)
- [53] U. Tradowsky, J. White, R.M. Ward, N. Read, W. Reimers, M.M. Attallah, *Mater. Des.* **105**, 212 (2016)
- [54] G.B. Eisaabadi, P. Davami, S.K. Kim, N. Varahram, *Mater. Sci. Eng. A* **552**, 36 (2012)
- [55] J. Zhang, J. Gao, B. Song, L. Zhang, C. Han, C. Cai, K. Zhou, Y. Shi, *Addit. Manuf.* **38**, 101829 (2021)
- [56] P. Skemer, I. Katayama, Z. Jiang, S.I. Karato, *Tectonophysics* **411**, 157 (2005)
- [57] S. Li, H. Hassanin, M.M. Attallah, N.J.E. Adkins, K. Essa, *Acta Mater.* **105**, 9 (2016)
- [58] L. Liu, Q. Ding, Y. Zhong, J. Zou, J. Wu, Y.L. Chiu, J. Li, Z. Zhang, Q. Yu, Z. Shen, *Mater. Today* **21**, 354 (2018)
- [59] M.-S. Pham, B. Dovggy, P.A. Hooper, C.M. Gourlay, A. Piglione, *Nat. Commun.* **11**, 749 (2020)
- [60] Y.M. Wang, T. Voisin, J.T. McKeown, J. Ye, N.P. Calt, Z. Li, Z. Zeng, Y. Zhang, W. Chen, T.T. Roehling, R.T. Ott, M.K. Santala, P.J. Depond, M.J. Matthews, A.V. Hamza, T. Zhu, *Nat. Mater.* **17**, 63 (2018)
- [61] X. Nie, H. Zhang, H. Zhu, Z. Hu, L. Ke, X. Zeng, *J. Alloys Compd.* **764**, 977 (2018)
- [62] Y. Qi, H. Zhang, X. Nie, Z. Hu, H. Zhu, X. Zeng, *Addit. Manuf.* **35**, 101346 (2020)
- [63] M. Calcagnotto, D. Ponge, E. Demir, D. Raabe, *Mater. Sci. Eng. A* **527**, 2738 (2010)
- [64] B. Cao, S.P. Joshi, K.T. Ramesh, *Scr. Mater.* **60**, 619 (2009)
- [65] D. Wang, C. Song, Y. Yang, Y. Bai, *Mater. Des.* **100**, 291 (2016)
- [66] Y. Kok, X.P. Tan, P. Wang, M.L.S. Nai, N.H. Loh, E. Liu, S.B. Tor, *Mater. Des.* **139**, 565 (2018)
- [67] S. Wang, C. Li, M. Yan, W. Bian, S. Wang, *Acta Metall. Sin. -Engl. Lett.* **3**, 104 (2009)
- [68] G. Wu, K. Dash, M.L. Galano, K.A.Q. O'Reilly, *Corros. Sci.* **157**, 41 (2019)
- [69] P.M. Smith, M.J. Aziz, *Acta Metall. Mater.* **42**, 3515 (1994)
- [70] J. Geng, G. Liu, T. Hong, M. Wang, D. Chen, N. Ma, H. Wang, *J. Alloys Compd.* **775**, 193 (2019)
- [71] R. Sampson, R. Lancaster, M. Sutcliffe, D. Carswell, C. Hauser, J. Barras, *Opt. Laser Technol.* **127**, 106194 (2020)
- [72] X.P. Li, G. Ji, Z. Chen, A. Addad, Y. Wu, H.W. Wang, J. Vleugels, J. Van Humbeeck, J.P. Kruth, *Acta Mater.* **129**, 183 (2017)
- [73] C. Wu, K. Ma, D. Zhang, J. Wu, S. Xiong, G. Luo, J. Zhang, F. Chen, Q. Shen, L. Zhang, E.J. Lavernia, *Sci. Rep.* **7**, 9589 (2017)
- [74] T. Chung, Y. Yang, C. Hsiao, W. Li, B. Huang, C. Tsao, Z. Shi, J. Lin, P.E. Fischione, T. Ohmura, J. Yang, *Int. J. Lightweight Mater. Manuf.* **1**, 142 (2018)
- [75] M. Karlik, B. Jouffrey, *Acta Mater.* **45**, 3251 (1997)
- [76] P.C. Bai, F. Liu, X.H. Hou, C.W. Zhao, Y.M. Xing, *Phys. Rev. B Condens. Matter* **407**, 4466 (2012)
- [77] T. Shanmugasundaram, M. Heilmaier, B.S. Murty, V.S. Sarma, *Mater. Sci. Eng. A* **527**, 7821 (2010)
- [78] Z. Yuan, Y. Tu, T. Yuan, Y. Zhang, Y. Huang, *J. Alloys Compd.* **859**, 157752 (2021)
- [79] M. Baucio, *ASM Metals Reference Book* (ASM International, Ohio, 1993)
- [80] N. Hansen, *Scr. Mater.* **51**, 801 (2004)
- [81] K. Matsuura, T. Ohmi, M. Kudoh, H. Takahashi, H. Kinoshita, K. Suzuki, *Metall. Mater. Trans. A* **35**, 333 (2004)
- [82] F. Barlat, M.V. Glazov, J.C. Brem, D.J. Lege, *Int. J. Plast.* **18**, 919 (2002)
- [83] B. Cai, B. Liu, S. Kabra, Y. Wang, K. Yan, P.D. Lee, Y. Liu, *Acta Mater.* **127**, 471 (2017)
- [84] M.X. Yang, F.P. Yuan, Q.G. Xie, Y.D. Wang, E. Ma, X.L. Wu, *Acta Mater.* **109**, 213 (2016)
- [85] A. Dutta, D. Ponge, S. Sandl bes, D. Raabe, *Materialia* **5**, 100252 (2019)
- [86] M. Ameli, B. Agnew, P.S. Leung, B. Ng, C.J. Sutcliffe, J. Singh, R. McGlen, *Appl. Therm. Eng.* **52**, 498 (2013)
- [87] B.P. Croom, H. Jin, P.J. Noell, B.L. Boyce, X. Li, *Acta Mater.* **181**, 377 (2019)